
Long-term Simulations of Multi-Dimensional Core-collapse Supernovae: Implications for Neutron Star Kicks

Ko NAKAMURA^{1,2*}, Tomoya TAKIWAKI,³ and Kei KOTAKE^{1,2}

¹Department of Applied Physics, Fukuoka University, Nanakuma 8-19-1, Johnan, Fukuoka 814-0180, Japan

²Research Institute of Stellar Explosive Phenomena, Fukuoka University, Nanakuma 8-19-1, Johnan, Fukuoka 814-0180, Japan

³Division of Theoretical Astronomy, National Astronomical Observatory of Japan, 2-21-1, Mitaka, Tokyo 181-8588, Japan

*E-mail: nakamurako@fukuoka-u.ac.jp

Received ; Accepted

Abstract

Core-collapse supernovae (CCSNe) are the final stage of massive stars, marking the birth of neutron stars (NSs). The aspherical mass ejection drives a natal kick of the forming NS. In this work we study the properties of the NS kick based on our long-term hydrodynamics CCSN simulations. We perform two-dimensional (2D) simulations for ten progenitors from a 10.8 to 20 M_{\odot} star covering a wide range of the progenitor's compactness parameter, and two three-dimensional (3D) simulations for an 11.2 M_{\odot} star. Our 2D models present a variety of explosion energies between $\sim 1.3 \times 10^{50}$ erg and $\sim 1.2 \times 10^{51}$ erg, and NS kick velocities between ~ 100 km s⁻¹ and ~ 1500 km s⁻¹. For the 2D exploding models, we find that the kick velocities tend to become higher with the progenitor's compactness. This is because the high progenitor compactness results in high neutrino luminosity from the proto-neutron star (PNS), leading to more energetic explosions. Since high-compactness progenitors produce massive PNSs, we point out that the NS masses and the kick velocities can be correlated, which is moderately supported by observation. Comparing 2D and 3D models of the 11.2 M_{\odot} star, the diagnostic explosion energy in 3D is, as previously identified, higher than that in 2D, whereas the 3D model results in a smaller asymmetry in the ejecta distribution and a smaller kick velocity than in 2D. Our results confirm the importance of self-consistent CCSN modeling covering a long-term postbounce evolution in 3D for a quantitative prediction of the NS kicks.

Key words: hydrodynamics - supernovae: general - stars: neutron

1 Introduction

Young radio pulsars have been measured to possess average velocities as high as 200-500 km s⁻¹ (e.g., Lyne & Lorimer 1994; Kaspi et al. 1996; Arzoumanian et al. 2002; Hobbs et al. 2005). Some of them have kick velocities higher than 500 km s⁻¹, such as the compact remnant RX J0822-4300 in Puppis A and PSR B1508+55 (e.g., Katsuda et al. (2018) for collective

references therein). It has long been proposed that these high kick velocities could be produced by asymmetric mass ejection when a core-collapse supernova (CCSN) explosion is initiated in a non-spherical manner (“hydrodynamic kick scenario”, e.g., Janka & Müller 1994; Burrows & Hayes 1996) or by anisotropic neutrino emission from the proto-neutron star (PNS; “neutrino-induced kick scenario”, e.g., Woosley 1987; Bisnovatyi-Kogan

1993; Lai et al. 2001; Kotake et al. 2005; Fryer & Kusenko 2006; Kusenko et al. 2008; Sagert & Schaffner-Bielich 2008).

In the hydrodynamic kick scenario, the non-radial instabilities (convective overturn and the standing accretion shock instability, SASI: (Blondin et al. 2003; Foglizzo et al. 2006, 2007)) play a key role in producing mass ejection asymmetries during the onset of the neutrino-driven explosion (see Janka et al. (2016) for a review). This has been demonstrated by two-dimensional (2D) and three-dimensional (3D) hydrodynamics simulations showing that the kick velocities can be as high as $\sim 1000 \text{ km s}^{-1}$ (e.g., Scheck et al. 2004, 2006; Nordhaus et al. 2010, 2012; Wongwathanarat et al. 2013; Janka 2017; Müller et al. 2017a). The kick velocities are generally imparted opposite to the direction of the stronger explosion, where the explosively nucleosynthesized elements are preferentially expelled (Wongwathanarat et al. 2013). Based on three-dimensional simulations, Wongwathanarat et al. (2013) were the first to propose that the forming NS is accelerated via the “gravitational tugboat mechanism,” whereby the asymmetric ejecta exerts a long-lasting momentum transfer to the NS by the gravitational pull over a period of seconds.

In fact, recent systematic measurements of X-ray morphologies for Galactic supernova remnants (SNRs) support the hydrodynamic kick scenario. They present evidence that the bulk of the supernova ejecta moves in the opposite directions to the proper motion of the NSs (Holland-Ashford et al. 2017; Bear & Soker 2018; Katsuda et al. 2018). For example, detailed X-ray mapping of Cas A and G292.0+1.8 has revealed that the bulk motion of the total ejecta is roughly in the opposite direction to the apparent motion of the NS. In the Puppis A SNR, optical fast-moving oxygen-rich knots were observed in the opposite direction to the proper motion of the NS. No correlation was observed between the kick velocities and the magnetic field strengths of the NSs (Katsuda et al. 2018), which conflicts with the neutrino-induced kick scenario assuming extremely strong NS magnetic fields ($\geq 10^{16} \text{ G}$).

In the seminal works by Scheck et al. (2004, 2006) and Wongwathanarat et al. (2013), it was shown that the kick velocities are connected to explosion properties such as the explosion energy and the mass of the ejected material and the central remnant. In order to clarify the connection between the explosion properties and the progenitor structure, one needs self-consistent supernova models. In the above studies, limited progenitors were employed ($15 M_{\odot}$ and $20 M_{\odot}$), where the central core was excised to follow the long-term evolution (see also Gessner & Janka (2018)). In the context of self-consistent simulations (Nordhaus et al. 2012; Bruenn et al. 2013; Müller 2015; Pan et al. 2016; Summa et al. 2016; Müller et al. 2017a; Vartanyan et al. 2018; O’Connor & Couch 2018), the progenitor dependence on the NS kick has not yet been studied. It should be mentioned that Janka (2017) investigated how the neutron

star kick depends on the energy, ejecta mass, and asymmetry of the supernova explosion based on an analytical scaling relation (see also Bray & Eldridge (2016, 2018)). These estimates should be validated by outcomes from self-consistent simulations.

Very recently Müller et al. (2019) presented 3D CCSN simulations of low-mass (low-compactness) progenitors until 1–2 s after bounce and proposed a possible correlation between kick velocity and some explosion properties. In this paper we present results of 2D CCSN simulations of $10.8 M_{\odot}$ – $20.0 M_{\odot}$ stars of Woosley et al. (2002) for longer-term post-bounce evolution covering a wide range of the progenitor’s compactness parameter. We pay attention to the progenitor’s compactness parameter ξ (O’Connor & Ott 2011) because it has been shown as one of the key parameters for diagnosing the explosion properties in both 1D (O’Connor & Ott 2011, 2013; Ugliano et al. 2012; Ertl et al. 2016; Sukhbold et al. 2016) and 2D models (Nakamura et al. 2015; Summa et al. 2016). In order to obtain a saturated value of the explosion energy, we had to follow a long-term evolution up to $\sim 7 \text{ s}$ after bounce of a $17 M_{\odot}$ star in 2D (e.g., Nakamura et al. (2016)). Given the computational cost, we employ the similar numerical scheme to Nakamura et al. (2015) where the isotropic diffusion source approximation (IDSA, Liebendörfer et al. (2009)) is used for spectral transport of electron and anti-electron neutrinos and a leakage scheme is employed for heavy lepton neutrinos¹. Since a large explosion asymmetry has been seen in recent 3D CCSN models (Hanke et al. 2013; Takiwaki et al. 2014; Abdikamalov et al. 2015; Lentz et al. 2015; Melson et al. 2015a; Takiwaki et al. 2016; Roberts et al. 2016; Müller et al. 2017b; Kuroda et al. 2017; Takiwaki & Kotake 2018; O’Connor & Couch 2018; Ott et al. 2018; Glas et al. 2018; Vartanyan et al. 2019; Burrows et al. 2019), we also perform a 3D simulation for an $11.2 M_{\odot}$ progenitor star (this progenitor model was also employed in Müller (2015)). We compare the kick properties with those from the corresponding 2D model.

This paper is organized as follows. Section 2 summarizes our numerical methods and the progenitor models employed in this work. We present our 2D and 3D results in Sections 3 and 4, respectively. We conclude with discussions in Section 5. In the Appendix 1 we present a caveat for the 2D models. Unless otherwise stated, time is measured after bounce throughout this paper.

2 Method

We employ ten progenitors from Woosley et al. (2002) covering zero-age main-sequence (ZAMS) masses from $10.8 M_{\odot}$

¹ Note that our updated code (Kotake et al. 2018) that can deal with three flavor neutrino transport with more detailed neutrino opacities is unfortunately too computationally expensive for the purpose of this work.

to $20.0 M_{\odot}$. All of the progenitors were trending towards an explosion in our previous 2D simulations covering ~ 1 s after bounce (Nakamura et al. 2015). In this paper we show the shock evolution up to a later post-bounce time (~ 8 s) in 2D. One of the progenitors is also simulated in 3D. Given that the progenitor's compactness parameter ξ_M , which is defined in O'Connor & Ott (2011) as a function of an enclosed mass M ,

$$\xi_M = \frac{M/M_{\odot}}{R(M)/1000\text{km}}, \quad (1)$$

is a good diagnostics for the explosion properties. The ten progenitors are taken to cover low to high ξ_M among the exploding models. The progenitor properties are summarized in Table 1. In this paper we estimate the compactness parameter ξ_M at $M = 2.5 M_{\odot}$ from the progenitor models.

The Newtonian hydrodynamics code that we employ in this work is essentially the same as that in Nakamura et al. (2015) except for some minor revisions. To follow a long-term evolution, the spatial range of the computational domain is extended from 5,000 km in radius to 100,000 km in this 2D study. The outer boundaries of all the models examined are located in the carbon-helium layers. The computational domain is sufficiently large to prevent the SN shock from being affected by the boundary condition before shock revival. The 2D models are computed on a spherical coordinate grid with a resolution of $n_r \times n_{\theta} = 1008 \times 128$ zones. For 3D models, we put the outer boundary at 10,000 km and simulate with the resolution of $n_r \times n_{\theta} \times n_{\phi} = 648 \times 64 \times 128$ zones. Our spatial grid has a finest mesh spacing $dr_{\min} = 250$ m at the center, and dr/r is better than 1.0 % at $r > 100$ km. Seed perturbations for aspherical instabilities are imposed by hand at 10 ms after bounce by introducing random perturbations of 0.1% in density on the whole computational grid except for the unshocked core.

For electron and anti-electron neutrinos, we employ the isotropic diffusion source approximation (IDSA, Liebendörfer et al. 2009), taking 20 energy bins with an upper bound of 300 MeV. For heavy-lepton neutrinos a leakage scheme is employed (see Nakamura et al. (2015) for more detail). Regarding the equation of state (EOS), we use that of Lattimer & Swesty (1991) with a nuclear incompressibility of $K = 220$ MeV. At low densities, we employ an EOS accounting for photons, electrons, positrons, and ideal gas contribution. We follow the explosive nucleosynthesis by solving a simple nuclear network consisting of 13 alpha-nuclei: ${}^4\text{He}$, ${}^{12}\text{C}$, ${}^{16}\text{O}$, ${}^{20}\text{Ne}$, ${}^{24}\text{Mg}$, ${}^{28}\text{Si}$, ${}^{32}\text{S}$, ${}^{36}\text{Ar}$, ${}^{40}\text{Ca}$, ${}^{44}\text{Ti}$, ${}^{48}\text{Cr}$, ${}^{52}\text{Fe}$, and ${}^{56}\text{Ni}$. Feedback from the composition change to the EOS is neglected, whereas the energy feedback from the nuclear reactions to the hydrodynamic evolution is taken into account as in Nakamura et al. (2014).

Note that our simulations exploit Newtonian gravity, which is inadequate for accurate modeling of CCSNe. The main goal of this series of systematic CCSN study (Nakamura et al. 2015; Horiuchi et al. 2017, 2018) is to explore qualitative properties

of CCSNe using self-consistent models. More sophisticated CCSN modeling with general relativistic effects is necessary for an accurate prediction of CCSN properties, including the NS kick. Our 3D CCSN simulations taking account of general relativistic effects will be reported in a forthcoming paper.

3 Results from 2D simulations

In this section we estimate the kick velocities of the (forming) NSs in our 2D models and attempt to compare them with observations. As is well known, the 2D assumption leads to an artificially powerful kick along the symmetry axis, making a quantitative comparison between models and observations difficult. However, we start from 2D models because qualitative discussions about the progenitor dependence of the kick velocities is yet to be explored even in (the context of self-consistent) 2D modeling, which we think still meaningful.

3.1 Neutron star kick

Our numerical code (grid setup) does not conserve the momentum and is unable to directly observe the central NS motion. More sophisticated methods employed by Nordhaus et al. (2010) and Nagakura et al. (2017) make it possible. A simple method to estimate NS kick velocity is to sum the net momentum of ejecta and convert it into a recoil velocity assuming momentum conservation. Another way to evaluate the kick velocity in such a momentum-non-conserving simulation is to integrate forces acting on the PNS. The kick velocity evaluated by force integration is, however, not so different from the recoil velocity given by a simple formula (Wongwathanarat et al. 2013). Therefore, we use the simple recoil formula (Scheck et al. 2004) in the current paper.

Following Scheck et al. (2004), we estimate the asymmetry of the ejected matter by α_{gas} ,

$$\alpha_{\text{gas}} \equiv |P_{z,\text{gas}}|/P_{\text{gas}} \equiv \left| \int dm v_z / \int dm |\vec{v}| \right|, \quad (2)$$

where $P_{z,\text{gas}}$ is the z -component (along the 2D axis) of the total momentum (P_{gas}) of the ejecta, v_z is the fluid velocity (v) along the axis, and m denotes the mass coordinates. The integrals are performed over the ‘‘ejecta’’ mass with the positive local energy and positive radial velocity at each time.

The kick velocity, v_{NS} , is estimated using α_{gas} as

$$v_{\text{NS}} = \alpha_{\text{gas}} P_{\text{gas}} / M_{\text{NS}}, \quad (3)$$

where the NS surface is defined at a fiducial density of $\rho = 10^{11} \text{ g cm}^{-3}$ and the baryonic NS mass (M_{NS}) is estimated by the enclosed mass.

Figure 1 shows the time evolution of v_{NS} for all the 2D models in this work. It shows a wide variety from $v_{\text{NS}} \sim 100 \text{ km s}^{-1}$ (model s11.0) to $\sim 850 \text{ km s}^{-1}$ (model s17.0) at the fi-

Table 1. Summary of the initial models in this work. All the progenitor models are taken from Woosley et al. (2002). Model name denotes solar metallicity (s) and zero-age main sequence mass in units of solar mass. Progenitor mass and radius, as well as Fe core mass and radius (M_{Fe} , R_{Fe}), the interface radius between CO and HeC layers ($R_{\text{CO/HeC}}$), and the mass included in the computational domain (M_{comp}) are listed. The compactness parameter ($\xi_{2.5}$) is estimated at $M = 2.5 M_{\odot}$ from the pre-collapse progenitor data.

Progenitor	Mass (M_{\odot})	Radius (R_{\odot})	M_{Fe} (M_{\odot})	R_{Fe} (km)	$R_{\text{CO/HeC}}$ (km)	M_{comp} (M_{\odot})	$\xi_{2.5}$
s10.8	10.4	563	1.36	1560	17800	1.82	0.003
s11.0	10.6	587	1.37	1460	25400	1.87	0.004
s11.2	10.8	596	1.25	1000	33500	1.91	0.005
s12.4	11.0	680	1.45	1590	34500	2.55	0.028
s13.8	11.8	774	1.48	1590	40600	3.03	0.081
s16.0	13.2	913	1.44	1580	50900	3.69	0.154
s17.0	13.8	958	1.44	1500	54400	4.06	0.161
s19.6	13.4	1160	1.47	1570	88600	5.04	0.119
s19.8	14.5	1130	1.44	1500	80700	5.02	0.136
s20.0	14.7	1120	1.46	1690	84200	5.10	0.127

nal simulation time. Note that the kick velocities from most of the 2D models are as fast as young radio pulsars (several hundred km s^{-1}). For models s11.0 and s17.0, the kick velocity (v_{NS}) temporarily becomes zero a few seconds after bounce. This is because the shock expansion of these models first occurs along one direction then transits to other direction (which we will discuss with reference to Figure 3). The shock revival occurs earliest for model s11.2 (thick blue dashed line) among the 2D models, which shows the earliest rise in v_{NS} ; however, the final value is relatively small among the models.

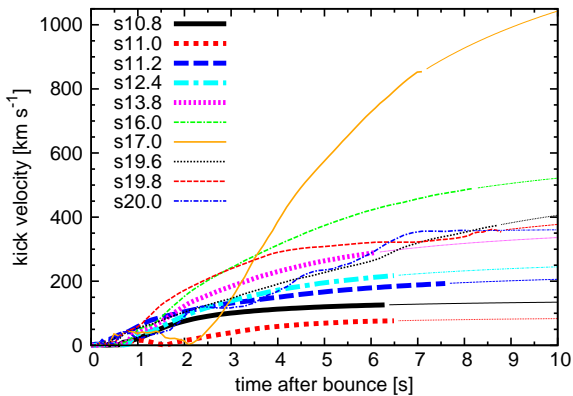


Fig. 1. Time evolution of the kick velocity in the 2D models. At the final time of our simulations, the kick velocity is mostly in the range $\sim 200 - 400 \text{ km s}^{-1}$, whereas it has a wide variety between $\sim 100 \text{ km s}^{-1}$ (slowest one for model s11.0, thick red dotted line) and $\sim 850 \text{ km s}^{-1}$ (fastest one for model s17.0, orange solid line) at the time each simulation terminates. We use Equation (4) and extrapolate the kick beyond the final simulation time (thin lines).

The v_{NS} estimated from Equation (3) is determined by α_{gas} , P_{gas} , and M_{NS} . The total momentum of ejecta P_{gas} is tightly connected to the vigorousness of explosion, or the explosion energy. The diagnostic explosion energy of our 2D models is

shown in the left panel of Figure 2. Here, the diagnostic energy is defined as the sum of the total energy (kinetic, internal and gravitational energies) in the “ejecta” region where the total energy and radial velocity are positive. Comparing with Figure 1, one can see that the diagnostic energies show a similar evolution to the kick velocity, which implies that P_{gas} is the dominant factor in the estimation of v_{NS} in Equation (3).

On the other hand, the asymmetry parameter α_{gas} does not show such a clear correlation to v_{NS} . For example, the asymmetry parameter of model s11.2 (thick blue dotted line) is almost converged at $\alpha_{\text{gas}} \sim 0.3$, which is very close to that of model s20.0 (thin blue dash-dotted line), whereas the kick velocity of model s11.2 is much smaller than that of model s20.0 (350 km s^{-1} , Figure 1). This is caused by the less energetic explosion of model s11.2, which results in a smaller value of the integrated gas momentum P_{gas} .

It should be noted that the models showing a unipolar explosion result in higher α_{gas} than those showing a bipolar explosion. Figure 3 depicts the evolution of the blast geometry for representative 2D models at 500 ms (left panels) and 2.5 s (right panels) after bounce, respectively. The shock of model s13.8 (middle-left panel in each plot of Figure 3), for example, is expanding to the northern direction, which results in high α_{gas} (thick magenta dotted line in Figure 2). On the other hand, bipolar explosion models (s11.0, s11.2, s17.0 and s20.0, see right panels of Figure 3) have smaller α_{gas} (0.1–0.25) compared with the other models ($\alpha_{\text{gas}} > 0.3$) at this time. Some of the models, s11.0 and s17.0, change the direction of the shock expansion during the long-term evolution. This leads to a significant change in the kick velocity as already mentioned (e.g., the zero-crossing feature in v_{NS} (Figure 1) as well as in α_{gas} (right panel of Figure 2)).

From Equation (3), the mass of the (forming) NS, M_{NS} , also

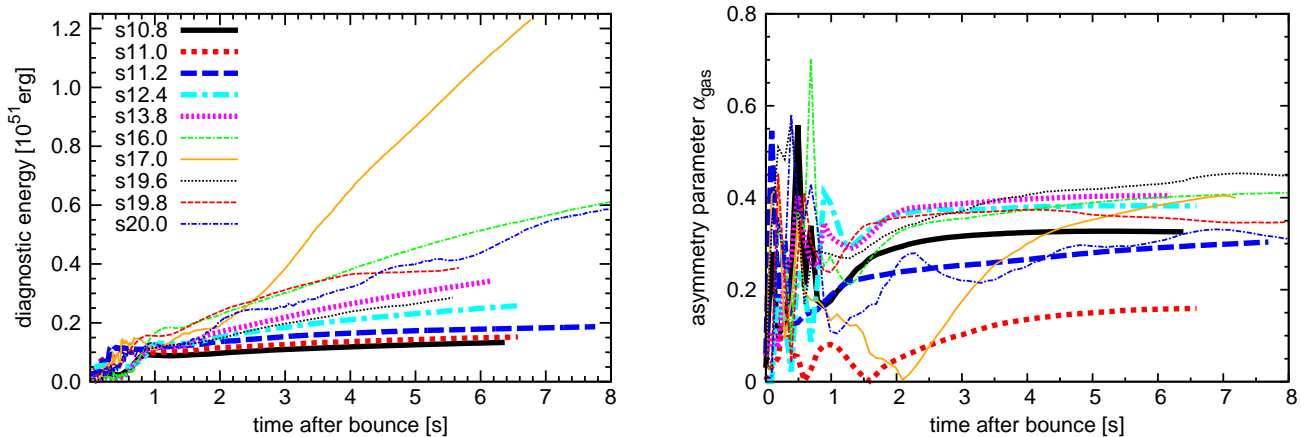


Fig. 2. Time evolutions of the diagnostic explosion energy (left panel) and the asymmetry parameter of the ejecta (α_{gas} , right panel), respectively. Note that the same line styles are used in both of the panels.

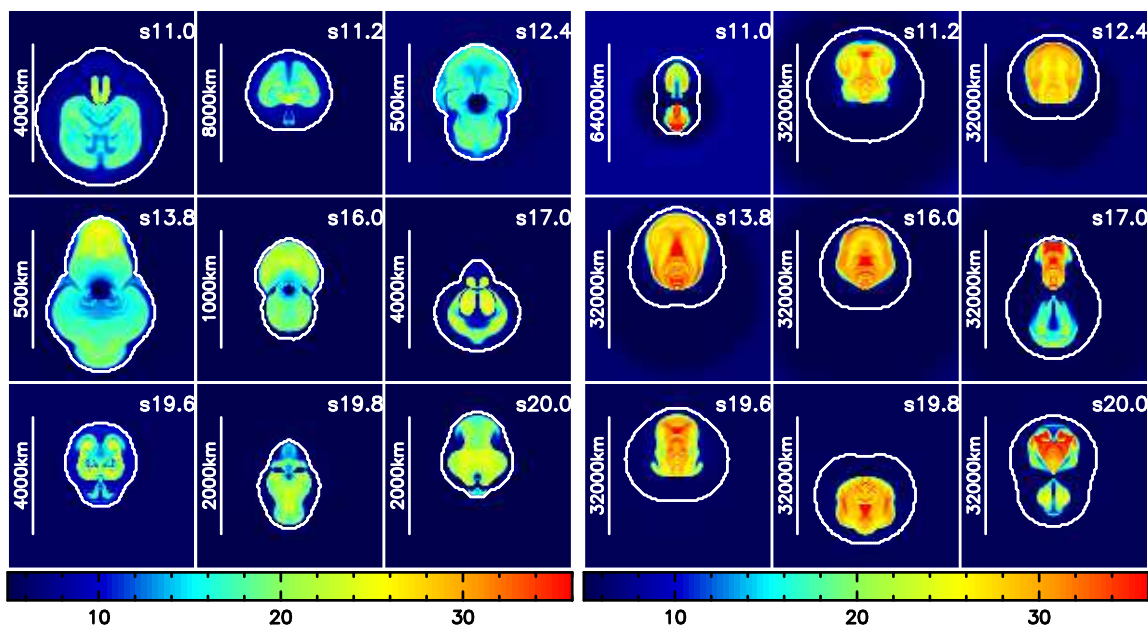


Fig. 3. Snapshots of the specific entropy s in k_B/baryon for nine models at 0.5 s (left panels) and 2.5 s (right panels) after bounce, respectively. The model name is denoted in the top right corner of each panel. Note the different spatial scale in each panel, which is indicated by the vertical scale bar. White lines surrounding the high-entropy region represent the position of shock waves. In the left panels, most of the models present a shock expansion, except for models s12.4 and s13.8 which still show a shock sloshing within ~ 250 km from the center. The right panels show that all of the models have a maximum shock radius larger than 10,000 km.

affects the kick velocity (v_{NS}). Figure 4 shows the evolution of the gravitational mass of the forming NS (left panel) with the average shock radius (right panel) in all the 2D models. By comparing the two panels, one can see that early shock revival (for example, model s11.2, thick blue dashed line) leads to the formation of a less massive NS. Note that the NS masses for models s10.8 (thick black solid line) and s12.4 (thick cyan dash-dotted line) are relatively small, although the shock revival time is late. This is because of the small mass accretion rate onto the PNS, which is characterized by the small progenitor's compactness parameter (see $\xi_{2.5}$ in Table 1). The NS masses of our 2D

models are in the range $1.65 \pm 0.3 M_{\odot}$, where the variation (at most $\sim 30\%$) is much smaller than that of v_{NS} . Our results suggest that the impact of M_{NS} on the kick velocity (see Equation (3)) is weaker compared to that of P_{gas} . Note again that P_{gas} is well correlated with the (diagnostic) explosion energy, as already mentioned. Therefore, small M_{NS} leads to small v_{NS} (not large v_{NS} , although M_{NS} is in the denominator of Equation (3)) because the small mass accretion rate to the PNS results in weaker explosion (via the small accretion neutrino luminosity), leading to a reduction in the total momentum of the ejecta (P_{gas}).

It should be noted that only three models (s10.8, s11.0, and s11.2), which have the smallest ZAMS mass and compactness among the examined models, leave a PNS with typical observational mass ($\sim 1.4 M_{\odot}$). The other models present higher M_{NS} ($> 1.6 M_{\odot}$) and it is still growing at the end of the simulations. Although standard initial mass functions (IMF), such as the Salpeter IMF, predict that heavy progenitors are subdominant, their too-massive PNS might be caused by some durable downflows peculiar to 2D axisymmetric simulations. This will be discussed in the Appendix 1 in detail.

3.2 Comparison with observation

As mentioned in the previous section, the kick velocity is predominantly determined by P_{gas} in Equation (3), or most equivalently by the strength of the explosion. Since the high progenitor compactness leads to the energetic explosion via the high (accretion) neutrino luminosity (Nakamura et al. 2015), one could imagine that there is a possible correlation between the progenitor's compactness parameter and the kick velocity.

The left panel of Figure 5 compares the kick velocities of our 2D models with the progenitor's compactness parameter $\xi_{2.5}$. We estimate the kick velocity at 5 s after bounce (filled circles), when the kick velocity is available for all the models given the different final simulation time. Also shown are the final values of the kick velocity (open circles) estimated by assuming $dv_{\text{NS}}/dt = at^{-2}$ (Müller et al. 2019), which gives the final kick velocity as

$$v_{\text{NS}}(t) = -at^{-1} + v_{\text{NS}}^{\text{f}}. \quad (4)$$

The parameter a and the final kick velocity v_{NS}^{f} are determined by fitting the simulation data over an interval of 0–1 s before the end of each simulation. Both of them show a rough correlation to the compactness. It may not be surprising that the kick velocity is also correlated with M_{NS} (right panel of Figure 5).

The progenitor's compactness parameter is, however, not directly observable. To get an idea of the relation between the NS mass and the kick velocity, we summarize in Table 2 the masses (Antoniadis et al. 2016, and references therein) of millisecond pulsars in a binary system and the tangential velocity of the proper motions obtained by radio timing observations and optical spectroscopy (Desvignes et al. 2016; Matthews et al. 2016). The table suggests that the more massive pulsars have a tendency to have a higher velocity. Readers should be aware that NSs in Table 2 had to maintain the binary system after the SN explosion they had once experienced. This means that their explosion was weak and/or the ejected mass was small, both of which could lead to smaller values of kick velocities compared with single NSs. Although more detailed analysis in order to clarify the relation between the observed proper motions and the NS natal kick is needed in order to draw a robust conclusion,

we point out that the correlation found in Figure 5 is compatible with the fact that the heaviest three NSs in Table 2 (J1909-3744, J0751+1807, and J1614-2230) have top-three kick velocities among the listed NSs. Here we do not include NS-NS binaries because they have undergone a second kick which obscures the possible correlation between NS kick and mass.

Table 3 summarizes some representative explosion properties of our 2D models such as the shock revival time, the diagnostic explosion energy, the mass of the PNS, the synthesized Ni mass, and the kick velocities. We define the shock revival time, t_{500} , as the time when an average shock radius reaches a radius of 500 km. Three kinds of kick velocities, v_{NS} , v_{NS}^* , and v_{NS}^{f} , are listed in the Table. v_{NS} is from our simulations (Figures 1 and 5), whereas v_{NS}^* is from a semi-analytical formula in Janka (2017),

$$v_{\text{NS}}^* = 211 \text{ km s}^{-1} \left(\frac{f_{\text{kin}}}{\epsilon_5 \beta_{\nu}} \right)^{1/2} \left(\frac{\alpha_{\text{gas}}}{0.1} \right) \left(\frac{E_{\text{dia}}}{10^{51} \text{ erg}} \right) \left(\frac{M_{\text{NS}}}{1.5 M_{\odot}} \right)^{-1}, \quad (5)$$

where α_{gas} and M_{NS} are the asymmetry parameter and baryonic NS mass as in Equation 3, and E_{dia} is the diagnostic explosion energy. We assume the second factor on the right-hand side including f_{kin} , the fraction of kinetic energy in the total explosion energy, to be unity (as suggested in Janka (2017)) and the other values are extracted from our simulations. Although v_{NS}^* can be $\sim 30\%$ smaller than v_{NS} , one can see that the analytical formula is able to quite nicely reproduce the main features of our results regarding the progenitor dependence of the kick velocities.

The values of the kick velocity in our 2D CCSN models range between 69 and 576 km s^{-1} at 5 s after bounce, ~ 100 and $\sim 850 \text{ km s}^{-1}$ at the final time of the simulations, and ~ 100 and $\sim 1500 \text{ km s}^{-1}$ in the estimated final values using Equation(4). Although this is, at least, compatible with the observed values (200–500 km s^{-1} for the youngest pulsars and $\sim 1000 \text{ km s}^{-1}$ for the fastest one), one should examine this in 3D models. However, 3D self-consistent, long-term CCSN simulations covering a wide range of progenitor mass (and compactness) are computationally very demanding. We shall limit ourselves to reporting two 3D runs, which we move on to explain in the next section.

Table 2. Pulsar properties

Name	Mass (M_{\odot})	velocity (km s^{-1})
J1918-0642	1.18	43
J1802-2124	1.24	13
B1855+09	1.30	42
J1713+0747	1.31	37
J1738+0333	1.47	60
J1909-3744	1.54	200
J0751+1807	1.64	85
J1614-2230	1.93	110

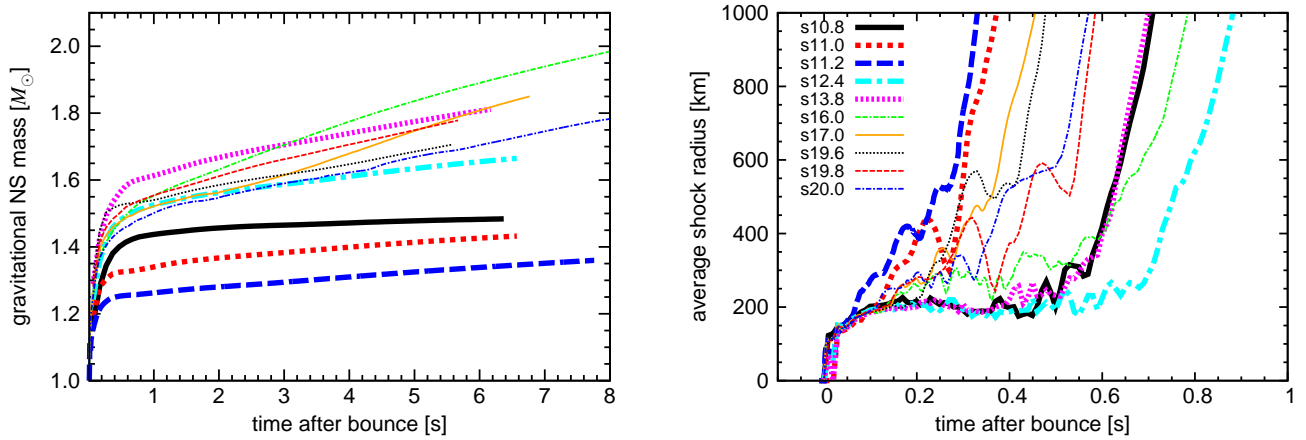


Fig. 4. Similar to Figure 3 but for the (gravitational) NS mass (left panel) and the average shock radius (right panel). Here, gravitational NS mass is defined as the rest mass, $\int \rho dV$, minus the mass equivalent of the binding energy, $\frac{1}{2} |\int \rho \Phi dV|$. Note in the right panel that only the post-bounce evolution up to 1 s is shown to focus on the shock revival time.

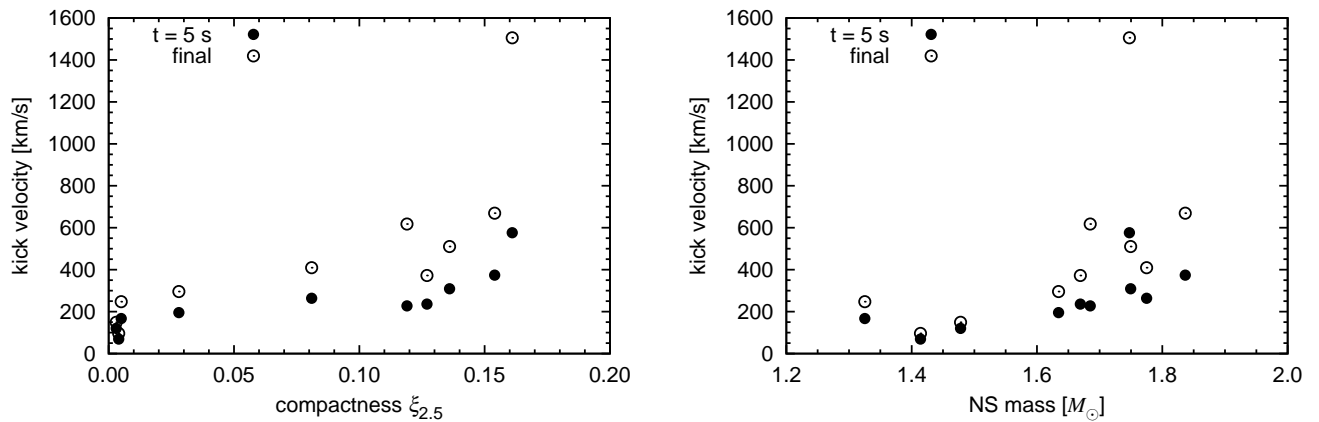


Fig. 5. NS kick velocity as a function of the compactness parameter $\xi_{2.5}$ (left panel) and gravitational NS mass (right panel). The kick velocities shown by filled circles, as well as NS mass in the right panel, are estimated at 5 s after bounce. The kick velocities shown by open circles are the estimated final values using Equation (4).

4 3D simulation of an $11.2M_{\odot}$ star

In this section we attempt to explore the long-term (> 1 s) evolution of a 3D model of a $11.2M_{\odot}$ star. To make this doable, we relax the Courant-Friedrichs-Lewy (CFL) condition by means of the “mesh coarsening” technique, by which one can significantly reduce the computational cost. In spherical coordinates, the CFL condition is quite severe around the polar axis, especially close to the center since the width of the numerical grid $\Delta l (= r \sin \frac{\theta}{2} d\phi \sim \frac{1}{2} r d\theta d\phi)$ becomes small there. To get around this problem, we combine the neighboring cells inside the PNS (“coarsen” the numerical grid) and make the timestep longer there by evaluating the timestep over the combined cells divided by the velocities averaged over the original cells (see Müller et al. (2019) for a more sophisticated mesh-coarsening scheme). The mesh coarsening level is arbitrary. We set the level to the maximum (1 zone in the θ - ϕ direction or spherical) within 10

km and then downgrade step by step (2×4 zones, 4×8 zones, to be in accordance with the original resolution). Apart from the use of mesh coarsening, the numerical code is the same for both 2D and 3D cases.

Figure 6 shows color-coded snapshots of the entropy for the 3D models of the $11.2 M_{\odot}$ star with (left panel) and without (right panel) the mesh coarsening. It can be seen that the 3D models have a nearly spherical shock structure, although the shock expansion in the model using mesh coarsening (left panel) tends to be aligned with the polar axis (the z axis in Figure 6). On the other hand, the model without mesh coarsening has a random distribution of high entropy regions behind the shock. Its shock front is deformed at this time but does not have a specific orientation, in stark contrast to our 3D model using mesh coarsening.

The left panel of Figure 7 compares the diagnostic explosion energy between the 3D models and the corresponding 2D

Table 3. Overview of explosion properties obtained in our 2D models. Shock revival time (t_{500}), diagnostic explosion energy (E_{dia}), gravitational NS mass (grav. M_{NS}), ejected Ni mass (M_{Ni}), and NS kick velocities (v_{NS} , v_{NS}^*) are estimated at 5 s after bounce. The final kick velocity (v_{NS}^f) is obtained from Equation (4).

Progenitor	t_{500} (s)	E_{dia} (foe)	grav. M_{NS} (M_{\odot})	M_{Ni} ($10^{-2} M_{\odot}$)	v_{NS} (km s^{-1})	v_{NS}^* (km s^{-1})	v_{NS}^f (km s^{-1})
s10.8	0.619	0.125	1.48	0.482	120	79	149
s11.0	0.300	0.143	1.41	0.503	69	43	96
s11.2	0.236	0.173	1.33	0.499	167	105	247
s12.4	0.760	0.232	1.63	0.638	195	151	296
s13.8	0.630	0.303	1.77	0.905	263	190	409
s16.0	0.641	0.452	1.84	1.36	374	265	669
s17.0	0.362	0.867	1.75	2.32	576	486	1505
s19.6	0.300	0.265	1.68	0.629	228	184	618
s19.8	0.450	0.374	1.75	0.878	309	216	510
s20.0	0.388	0.399	1.67	1.14	236	198	372

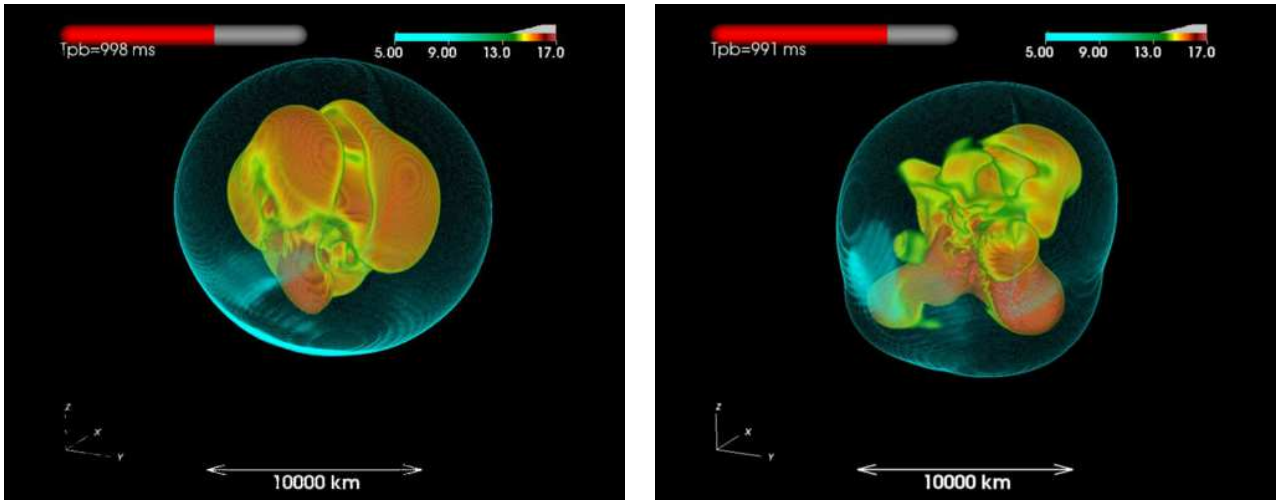


Fig. 6. 3D entropy maps of the $11.2 M_{\odot}$ model with (left panel) and without (right panel) the mesh coarsening scheme at ~ 1 s after bounce. The position of the shock is highlighted by a semitransparent surface colored by bright cyan for both of the models.

model. Our 3D models have higher explosion energy than the 2D model when their maximum shock radius reaches the outer boundary of the simulation regime (10,000 km, 1/10 of the 2D models) when the 3D runs are terminated. This is consistent with the result of Müller (2015), who employed the same progenitor model. The energetic explosion of the 3D models is driven by outflow from the central region. The right panel of Figure 7 presents the ratio of the mass outflow rate \dot{M}_{out} to the mass accretion rate \dot{M}_{acc} measured at a radius of 500 km. The 3D models evolve in a similar way to the 2D model until ~ 0.5 s after bounce, then \dot{M}_{out} increases to become comparable to \dot{M}_{acc} and the explosion energy of the 3D models overwhelms that of the 2D model. The flow ratio of the 2D model falls below unity at ~ 0.35 s and after that the explosion energy does not grow. The mass accretion rate of the 2D model becomes higher than the outflow rate, but small because of the small progeni-

tor's compactness in model s11.2, and the PNS mass increases slowly with time (Figure 4, left panel).

To estimate the kick properties from the 3D models, one needs to slightly modify equation (2) as $\alpha_{\text{gas}} \equiv |\vec{P}_{\text{gas}}|/P_{\text{gas}} \equiv |\int dm \vec{v}| / \int dm |\vec{v}|$. Among the 3D models, the model simulated with mesh coarsening (model 3Dc) has an oriented shock expansion and a larger explosion energy than the 3D model without mesh coarsening (model 3D). This results in its asymmetry parameter being as high as the corresponding 2D model (Figure 8, right panel) and the highest kick velocity among the models shown here (Figure 7, left panel). The kick velocity of the 2D model is 66 km s^{-1} at 1.1 s after bounce. The kick velocity of the 3Dc model at that time is $\sim 96 \text{ km s}^{-1}$, about 50 % higher (left panel of Figure 8). This is caused by a ~ 50 % larger explosion energy in the 3Dc model (1.7×10^{50} erg) than in the 2D model (1.2×10^{50} erg). On the other hand, the kick ve-

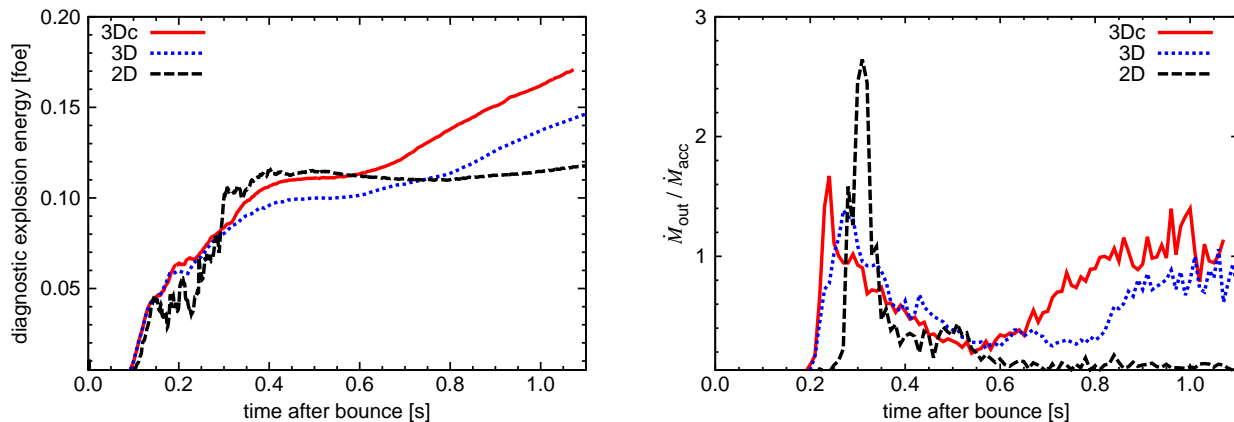


Fig. 7. The diagnostic explosion energy (left panel) and the ratio of the mass outflow rate \dot{M}_{out} to the mass accretion rate \dot{M}_{acc} (right panel) as a function of the post-bounce time. The mass flow rate is measured at a radius of 500 km. Shown are 3D models with and without mesh coarsening (labeled as 3Dc (red solid line) and 3D (blue dashed line), respectively) of the $11.2 M_{\odot}$ star compared with the corresponding 2D model (black dashed line).

licity of the 3D model without the coarsening method is small (14 km s^{-1} , 80 % smaller than the 2D kick), which is caused by the nearly spherical distribution of the ejecta (small α_{gas}). Our results demonstrate that the use of mesh coarsening, albeit quite useful for making long-term 3D runs possible, could make the shock expansion align closely along the polar axis, possibly leading to an overestimation of the kick velocity. It should be noted that CCSN properties such as NS kick velocity could be affected by the stochastic nature of nonlinear hydrodynamics. It is still unclear whether the disagreement between the two 3D models is caused by the mesh coarsening or merely a result of the stochasticity. Examined here is only one progenitor with a ZAMS mass of $11.2 M_{\odot}$, and the results might depend on the coarsening level as well as the progenitor structure. More detailed study is apparently needed to unambiguously pin down the impact of the mesh coarsening on the explosion properties in 3D CCSN models.

5 Summary and Discussion

We have investigated the properties of the kick velocities of the forming NSs based on our long-term hydrodynamics CCSN simulations. We performed 2D simulations for ten progenitors from a 10.8 to $20 M_{\odot}$ star covering a wide range of progenitor compactness parameter, and two 3D runs for an $11.2 M_{\odot}$ star. Our 2D models presented a variety of the explosion energies between $\sim 1.3 \times 10^{50}$ erg and $\sim 1.2 \times 10^{51}$ erg, and NS kick velocities between $\sim 100 \text{ km s}^{-1}$ and $\sim 1500 \text{ km s}^{-1}$. For the 2D exploding models, it was found that the total momentum of the ejecta, or the explosion energy, is a predominant factor determining the kick velocity, whereas the ejecta asymmetry and NS mass play a secondary role. We also found that the kick velocities tend to become higher with the progenitor's compactness. This is because high progenitor compactness re-

sults in high neutrino luminosity from the PNS, leading to more energetic explosions. Since the high-compactness progenitors produce massive PNS, we point out that the NS masses and the kick velocities can be correlated (very recently similar conclusion was obtained in Müller et al. (2019), see their Figure 12 for detail), which we point out is moderately supported by observation of pulsars in binary systems. Comparing the 2D and 3D models of the $11.2 M_{\odot}$ star, the diagnostic explosion energy in 3D is, as previously identified, higher than that in 2D, whereas the 3D model results in smaller asymmetry in the ejecta distribution and smaller kick velocity than in 2D. The kick velocity of the 3D model is ~ 80 % smaller than that of 2D model. We discussed some possible drawbacks of using the mesh coarsening to estimate the kick velocity.

Our CCSN models even in 2D do not reach typical SN observational values in terms of the smaller explosion energies (less than $\sim 10^{51}$ erg, except for model s17.0) and the level of the synthesized ^{56}Ni . Some possible missing ingredients to make the underpowered explosion more energetic (also in 3D) should include multi-dimensional effects during the final stage of the pre-supernova evolution (see Couch & Ott (2013); Fernández et al. (2014); Couch & Ott (2015); Müller & Janka (2015); Burrows et al. (2018); Yoshida et al. (2019)), general relativity (e.g., Müller et al. (2012); Ott et al. (2013); Kuroda et al. (2012, 2016)), rapid rotation and/or magnetic fields (e.g., Marek & Janka (2009); Suwa et al. (2010); Takiwaki et al. (2016); Summa et al. (2018); Harada et al. (2018); Obergaulinger et al. (2006); Mösta et al. (2014); Guilet & Müller (2015); Masada et al. (2015); Obergaulinger & Aloy (2017)), sophistication in the neutrino opacities (Melson et al. 2015b; Bollig et al. 2017; Burrows et al. 2018; Kotake et al. 2018) and the transport schemes (e.g., Sumiyoshi & Yamada (2012); Richers et al. (2017); Nagakura et al. (2018); Just et al. (2018)), and possibly inclusion of the quark-hadron phase transition in the center of

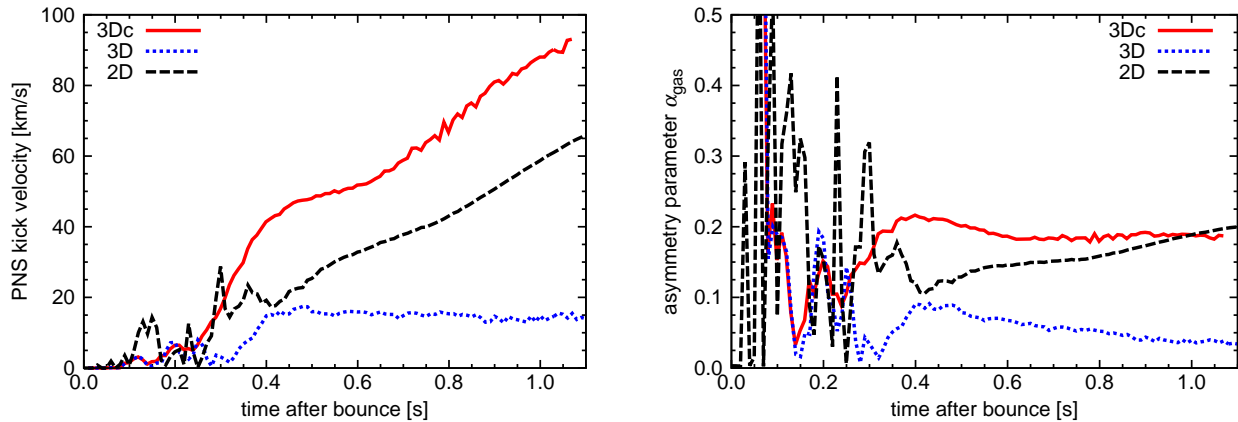


Fig. 8. Same as Figure 7 but for the kick velocity (left panel) and the asymmetry parameter (right panel).

the PNS (Fischer et al. 2018). As for predicting NS kicks, systematic study based on 3D CCSN modeling including a suite of the above missing facets is mandatory for making quantitative CCSN multi-messenger predictions possible. This study is nothing but a very first step toward the final goal.

Acknowledgments

We thank Masaomi Tanaka and Masaki Yamaguchi for helpful discussions. This study was supported in part by Grants-in-Aid for Scientific Research of the Japan Society for the Promotion of Science (JSPS, Nos. JP26707013, JP26870823, JP16K17668, JP17H01130, JP17K14306, JP18H01212), the Ministry of Education, Science and Culture of Japan (MEXT, Nos. JP15H00789, JP15H01039, JP15KK0173, JP17H05205, JP17H05206, JP17H06357, JP17H06364, JP17H06365, JP24103001, JP24103006, JP26104001, JP26104007), by the Central Research Institute of Explosive Stellar Phenomena (REISEP) at Fukuoka University and associated projects (Nos.171042,177103), and JICFuS as a priority issue to be tackled by using the Post “K” Computer. This work was also supported by the NINS program for cross-disciplinary study (Grant Numbers 01321802 and 01311904) on Turbulence, Transport, and Heating Dynamics in Laboratory and Solar/Astrophysical Plasmas: “SoLaBo-X”.

References

- Abdikamalov, E., Ott, C. D., Radice, D., et al. 2015, *ApJ*, 808, 70
- Antoniadis, J., Tauris, T. M., Ozel, F., et al. 2016, *ArXiv e-prints*, arXiv:1605.01665
- Arzoumanian, Z., Chernoff, D. F., & Cordes, J. M. 2002, *ApJ*, 568, 289
- Bear, E., & Soker, N. 2018, *ApJ*, 855, 82
- Bisnovatyi-Kogan, G. S. 1993, *Astronomical and Astrophysical Transactions*, 3, 287
- Blondin, J. M., Mezzacappa, A., & DeMarino, C. 2003, *ApJ*, 584, 971
- Bollig, R., Janka, H.-T., Lohs, A., et al. 2017, *Physical Review Letters*, 119, 242702
- Bray, J. C., & Eldridge, J. J. 2016, *MNRAS*, 461, 3747
- . 2018, *MNRAS*, 480, 5657
- Bruenn, S. W., Mezzacappa, A., Hix, W. R., et al. 2013, *ApJL*, 767, L6
- Burrows, A., & Hayes, J. 1996, *Physical Review Letters*, 76, 352
- Burrows, A., Radice, D., & Vartanyan, D. 2019, *MNRAS*, arXiv:1902.00547
- Burrows, A., Vartanyan, D., Dolence, J. C., Skinner, M. A., & Radice, D. 2018, *Space Sci. Rev.*, 214, 33
- Couch, S. M., & Ott, C. D. 2013, *ApJL*, 778, L7
- . 2015, *ApJ*, 799, 5
- Desvignes, G., Caballero, R. N., Lentati, L., et al. 2016, *MNRAS*, 458, 3341
- Ertl, T., Janka, H.-T., Woosley, S. E., Sukhbold, T., & Ugliano, M. 2016, *ApJ*, 818, 124
- Fernández, R., Müller, B., Foglizzo, T., & Janka, H.-T. 2014, *MNRAS*, 440, 2763
- Fischer, T., Bastian, N.-U. F., Wu, M.-R., et al. 2018, *Nature Astronomy*, 2, 980
- Foglizzo, T., Galletti, P., Scheck, L., & Janka, H.-T. 2007, *ApJ*, 654, 1006
- Foglizzo, T., Scheck, L., & Janka, H.-T. 2006, *ApJ*, 652, 1436
- Fryer, C. L., & Kusenko, A. 2006, *ApJS*, 163, 335
- Gessner, A., & Janka, H.-T. 2018, *ApJ*, 865, 61
- Glas, R., Just, O., Janka, H.-T., & Obergaulinger, M. 2018, *arXiv e-prints*, arXiv:1809.10146
- Guilet, J., & Müller, E. 2015, *MNRAS*, 450, 2153
- Hanke, F., Müller, B., Wongwathanarat, A., Marek, A., & Janka, H.-T. 2013, *ApJ*, 770, 66
- Harada, A., Nagakura, H., Iwakami, W., et al. 2018, *arXiv e-prints*, arXiv:1810.12316
- Hobbs, G., Lorimer, D. R., Lyne, A. G., & Kramer, M. 2005, *MNRAS*, 360, 974

- Holland-Ashford, T., Lopez, L. A., Auchettl, K., Temim, T., & Ramirez-Ruiz, E. 2017, *ApJ*, 844, 84
- Horiuchi, S., Nakamura, K., Takiwaki, T., & Kotake, K. 2017, *Journal of Physics G Nuclear Physics*, 44, 114001
- Horiuchi, S., Sumiyoshi, K., Nakamura, K., et al. 2018, *MNRAS*, 475, 1363
- Janka, H.-T. 2017, *ApJ*, 837, 84
- Janka, H.-T., Melson, T., & Summa, A. 2016, *Annual Review of Nuclear and Particle Science*, 66, 341
- Janka, H.-T., & Müller, E. 1994, *A&A*, 290, 496
- Just, O., Bollig, R., Janka, H.-T., et al. 2018, *MNRAS*, 481, 4786
- Kaspi, V. M., Bailes, M., Manchester, R. N., Stappers, B. W., & Bell, J. F. 1996, *Nature*, 381, 584
- Katsuda, S., Morii, M., Janka, H.-T., et al. 2018, *ApJ*, 856, 18
- Kotake, K., Takiwaki, T., Fischer, T., Nakamura, K., & Martínez-Pinedo, G. 2018, *ApJ*, 853, 170
- Kotake, K., Yamada, S., & Sato, K. 2005, *ApJ*, 618, 474
- Kuroda, T., Kotake, K., Hayama, K., & Takiwaki, T. 2017, *ApJ*, 851, 62
- Kuroda, T., Kotake, K., & Takiwaki, T. 2012, *ApJ*, 755, 11
- Kuroda, T., Takiwaki, T., & Kotake, K. 2016, *ApJS*, 222, 20
- Kusenko, A., Mandal, B. P., & Mukherjee, A. 2008, *Phys. Rev. D*, 77, 123009
- Lai, D., Chernoff, D. F., & Cordes, J. M. 2001, *ApJ*, 549, 1111
- Lattimer, J. M., & Swesty, F. D. 1991, *Nuclear Physics A*, 535, 331
- Lentz, E. J., Bruenn, S. W., Hix, W. R., et al. 2015, *ApJL*, 807, L31
- Liebendörfer, M., Whitehouse, S. C., & Fischer, T. 2009, *ApJ*, 698, 1174
- Lyne, A. G., & Lorimer, D. R. 1994, *Nature*, 369, 127
- Marek, A., & Janka, H.-T. 2009, *ApJ*, 694, 664
- Masada, Y., Takiwaki, T., & Kotake, K. 2015, *ApJL*, 798, L22
- Matthews, A. M., Nice, D. J., Fonseca, E., et al. 2016, *ApJ*, 818, 92
- Melson, T., Janka, H.-T., Bollig, R., et al. 2015a, *ApJL*, 808, L42
- . 2015b, *ApJL*, 808, L42
- Mösta, P., Richers, S., Ott, C. D., et al. 2014, *ArXiv e-prints*, arXiv:1403.1230
- Müller, B. 2015, *MNRAS*, 453, 287
- Müller, B., & Janka, H.-T. 2015, *MNRAS*, 448, 2141
- Müller, B., Janka, H.-T., & Marek, A. 2012, *ApJ*, 756, 84
- Müller, B., Melson, T., Heger, A., & Janka, H.-T. 2017a, *MNRAS*, 472, 491
- . 2017b, *MNRAS*, 472, 491
- Müller, B., Tauris, T. M., Heger, A., et al. 2019, *MNRAS*, 484, 3307
- Nagakura, H., Iwakami, W., Furusawa, S., et al. 2017, *ApJS*, 229, 42
- . 2018, *ApJ*, 854, 136
- Nakamura, K., Horiuchi, S., Tanaka, M., et al. 2016, *MNRAS*, 461, 3296
- Nakamura, K., Takiwaki, T., Kotake, K., & Nishimura, N. 2014, *ApJ*, 782, 91
- Nakamura, K., Takiwaki, T., Kuroda, T., & Kotake, K. 2015, *Publications of the Astronomical Society of Japan*, 67, 107
- Nordhaus, J., Brandt, T. D., Burrows, A., & Almgren, A. 2012, *MNRAS*, 423, 1805
- Nordhaus, J., Brandt, T. D., Burrows, A., Livne, E., & Ott, C. D. 2010, *Phys. Rev. D*, 82, 103016
- Obergaulinger, M., & Aloy, M. Á. 2017, *MNRAS*, 469, L43
- Obergaulinger, M., Aloy, M. A., Dimmelmeyer, H., & Müller, E. 2006, *Astron. Astrophys.*, 457, 209
- O'Connor, E., & Ott, C. D. 2011, *ApJ*, 730, 70
- . 2013, *ApJ*, 762, 126
- O'Connor, E. P., & Couch, S. M. 2018, *ApJ*, 854, 63
- O'Connor, E. P., & Couch, S. M. 2018, *ApJ*, 865, 81
- Ott, C. D., Roberts, L. F., da Silva Schneider, A., et al. 2018, *ApJL*, 855, L3
- Ott, C. D., Abdikamalov, E., Mösta, P., et al. 2013, *ApJ*, 768, 115
- Pan, K.-C., Liebendörfer, M., Hempel, M., & Thielemann, F.-K. 2016, *ApJ*, 817, 72
- Richers, S., Nagakura, H., Ott, C. D., et al. 2017, *ApJ*, 847, 133
- Roberts, L. F., Ott, C. D., Haas, R., et al. 2016, *ApJ*, 831, 98
- Sagert, I., & Schaffner-Bielich, J. 2008, *A&A*, 489, 281
- Scheck, L., Kifonidis, K., Janka, H.-T., & Müller, E. 2006, *A&A*, 457, 963
- Scheck, L., Plewa, T., Janka, H.-T., Kifonidis, K., & Müller, E. 2004, *Physical Review Letters*, 92, 011103
- Sukhbold, T., Ertl, T., Woosley, S. E., Brown, J. M., & Janka, H.-T. 2016, *ApJ*, 821, 38
- Sumiyoshi, K., & Yamada, S. 2012, *ApJS*, 199, 17
- Summa, A., Hanke, F., Janka, H.-T., et al. 2016, *ApJ*, 825, 6
- Summa, A., Janka, H.-T., Melson, T., & Marek, A. 2018, *ApJ*, 852, 28
- Suwa, Y., Kotake, K., Takiwaki, T., et al. 2010, *PASJ*, 62, L49
- Takiwaki, T., & Kotake, K. 2018, *MNRAS*, 475, L91
- Takiwaki, T., Kotake, K., & Suwa, Y. 2014, *ApJ*, 786, 83
- . 2016, *MNRAS*, 461, L112
- Ugliano, M., Janka, H.-T., Marek, A., & Arcones, A. 2012, *ApJ*, 757, 69
- Vartanyan, D., Burrows, A., Radice, D., Skinner, M. A., & Dolence, J. 2018, *MNRAS*, 477, 3091
- . 2019, *MNRAS*, 482, 351
- Wongwathanarat, A., Janka, H.-T., & Müller, E. 2013, *A&A*, 552, A126
- Woosley, S. E. 1987, in *IAU Symposium*, Vol. 125, *The Origin and Evolution of Neutron Stars*, ed. D. J. Helfand & J.-H. Huang, 255–270
- Woosley, S. E., Heger, A., & Weaver, T. A. 2002, *Reviews of Modern Physics*, 74, 1015
- Yoshida, T., Takiwaki, T., Kotake, K., et al. 2019, *arXiv e-prints*, arXiv:1903.07811

Appendix 1 Continuous Accretion in 2D models

In this Appendix we revisit a caveat for the 2D models with high progenitor compactness, in which a downflow to the PNS is liable to continue for a long time, making the PNS too massive to be compared with observed ones (see also the detailed analysis by Müller et al. (2012).)

The 2D models with smaller progenitor compactness (such as model 11.2 with $\xi_{2.5} = 0.005$, see Table 1) can get around this problem because of the small mass accretion and the early shock revival. Models s10.8 and s11.0 also have very small compactness compared to the others, and their PNS mass is also small (1.48 and $1.41 M_{\odot}$). The diagnostic explosion energy is also small for these three models ($1.25 - 1.73 \times 10^{50}$ erg). These results are consistent with the previous long-term 2D CCSN simulation by Müller (2015), where 2D simulations for progenitors in a similar mass range ($11.0 M_{\odot} - 11.6 M_{\odot}$) results in $1.3 M_{\odot} - 1.6 M_{\odot}$ PNS (baryonic) mass and $0.50 - 2.1 \times 10^{50}$ erg diagnostic energy.

For the 2D models with higher progenitor compactness, the PNS (gravitational) masses keep growing during the simulation and finally become higher than typical observational value ($\sim 1.4 M_{\odot}$). The PNSs of these models are exposed to continuous mass accretion even after shock revival. This can be seen from Figure 9, where the mass shell diagram for model s11.2 is compared with that of s17.0. These models show shock revival when the Si/SiO interface falls onto the shock. After the shock revival, the mass shells of model s11.2 is shown to turn to going outward and the mass accretion onto the PNS nearly stops. On the other hand, the mass accretion to the PNS continues even after the shock revival for model s17.0 (bottom panel).

To visualize this, we plot in Figure 10 snapshots of the radial velocity and the entropy in the central regions of these two models and of an additional model, s27.0. The central spherical regions with low entropy and nearly zero radial velocity correspond to the PNS. The PNS of model s11.2 (left panels) is surrounded by high-entropy gas heated by neutrinos. No clear long-lasting downflows to the PNS are observed. On the other hand, several strong downflows to the PNSs (colored by blue in the velocity plots) are clearly seen for models s17.0 (middle panels) and s27.0 (right panels). This feature is common to other 2D models with relatively high progenitor compactness. The infall flow wriggles around the PNS and, once it collides with its mirror flow on the symmetry axis, strong and durable down-flows from north and/or south poles to PNS are produced. Model s27.0, which has higher compactness ($\xi_{2.5} = 0.232$) than the models examined in this paper, leaves behind a central remnant with a gravitational mass of $2.27 M_{\odot}$ at the end of the simulation. This value is higher than the maximum mass of a cold NS ($2.04 M_{\odot}$) for the currently employed LS220 EOS, although thermal pressure can leverage the maximum PNS mass.

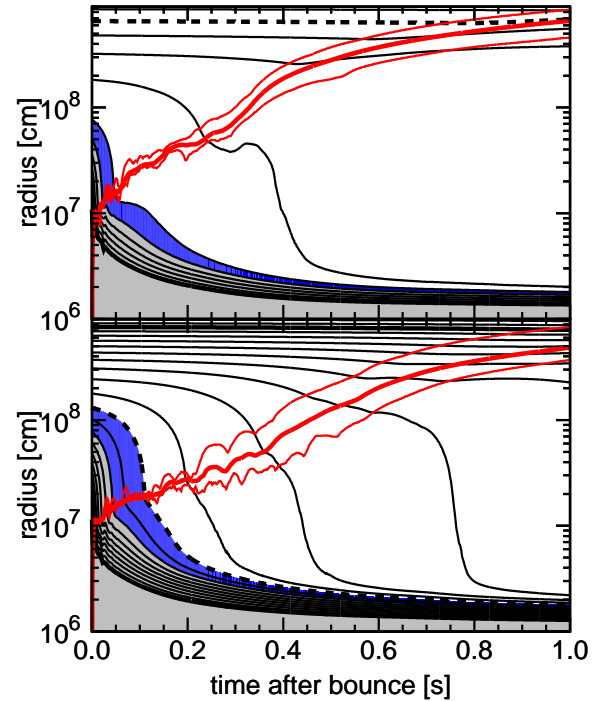


Fig. 9. Mass shell diagram for models s11.2 (top panel) and s17.0 (bottom panel). The thick black lines correspond to the mass coordinate at every $0.5 M_{\odot}$, with the thin lines at every $0.05 M_{\odot}$. The dashed lines show the mass coordinate of $1.5 M_{\odot}$ for reference. The color-shaded regions present the iron core (grey) and the silicon layer (blue) of each progenitor. The shock positions (red lines: maximum, average, and minimum from top to bottom) turn to go outward when the Si/SiO interface falls onto the shock.

To assess the fate of this heavy remnant, we refer to 1D general relativistic simulations by O’Connor & Ott (2011) using the same EOS. A linear fit to their results gives the maximum PNS mass as a function of the compactness (Nakamura et al. 2015),

$$M_{\text{PNS,max}}/M_{\odot} = 0.52\xi_{2.5} + 2.01. \quad (\text{A1})$$

This formula gives $M_{\text{PNS,max}} = 2.13 M_{\odot}$ for model s27.0, and implies black hole (BH) formation at 5.28 s, although our Newtonian simulation does not have the ability to follow the BH formation.

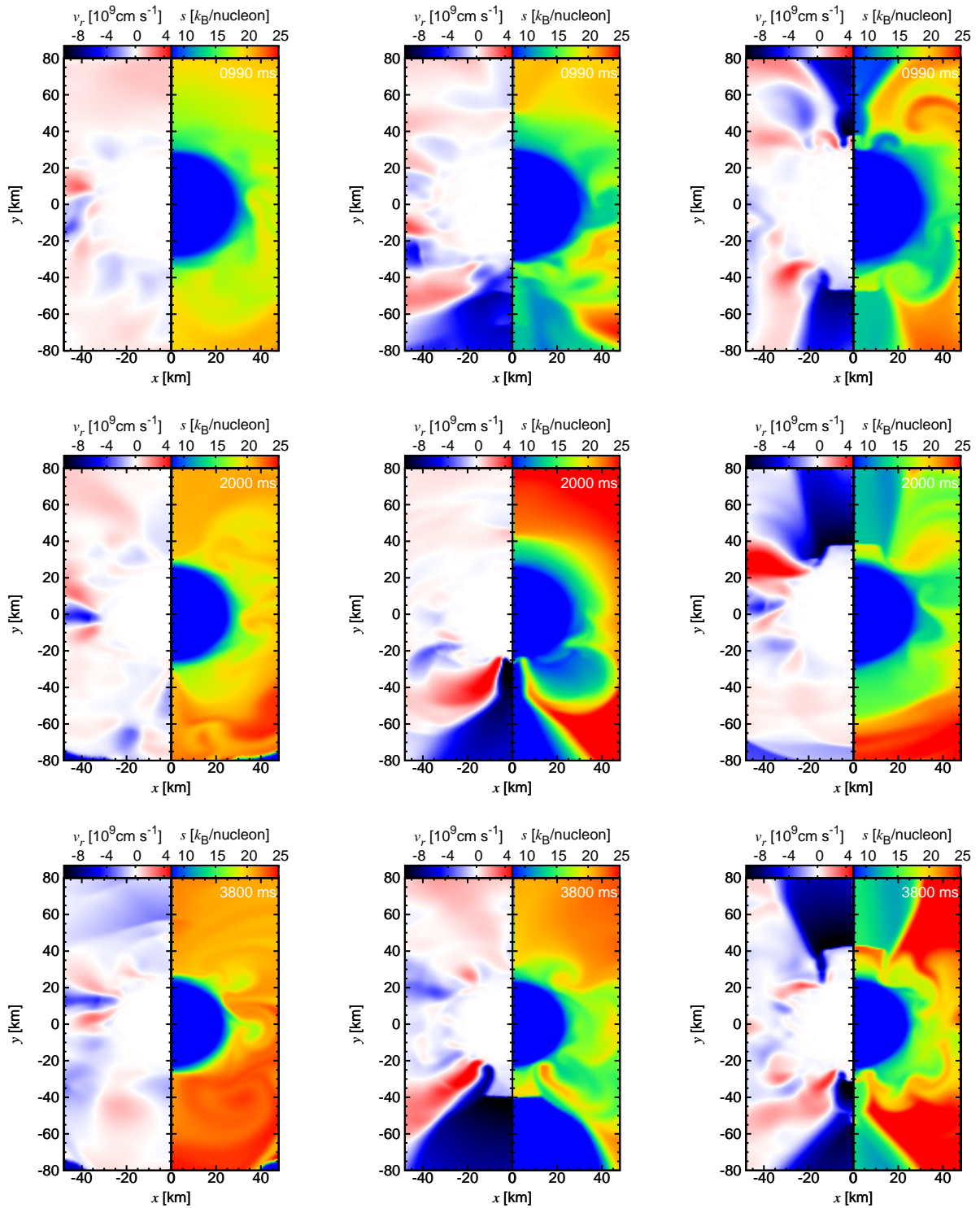


Fig. 10. Snapshots of the radial velocity v_r (left column of each panel, in 10^9 cm s^{-1}) and the specific entropy s (right column, in $k_B/\text{nucleon}$) for models s11.2 (left panels), s17.0 (middle panels), and s27.0 (right panels). Three time steps at post-bounce times of 990 ms, 2000 ms, and 3800 ms are shown from top to bottom. Note the absence of the low-entropy downflow onto the surface of the PNS for model s11.2 during a long-term simulation.